Light Water Reactor Sustainability Program

Development of Fast Fourier Transform (FFT) micro-mechanical simulations of concrete specimens characterized by micro-X-ray fluorescence

Alain Giorla

Development of Fast Fourier Transform (FFT) micro-mechanical simulations of concrete specimens characterized by micro-X-ray fluorescence

Alain Giorla

CONTENTS

LIST OF FIGURES

LIST OF TABLES

ACRONYMS

ASR   Alkali-Silica Reaction

CBS   Concrete Biological Shield

CT   X-Ray Computed Tomography

FEM   Finite Element Method

FFT   Fast Fourier Transform

IMAC   Irradiated Minerals, Aggregates and Concrete

LWRS   Light Water Reactor Sustainability

MOSAIC Microstructure-Oriented Scientific Analysis of Irradiated Concrete

μ-XRF   micro-X-Ray Fluorescence

NPP   Nuclear Power Plant

ORNL   Oak Ridge National Laboratory

RIVE   Radiation-Induced Volumetric Expansion

XML   Extensible Markup Language

EXECUTIVE SUMMARY

Concrete in Nuclear Power Plants (NPPs) can be exposed to a wide range of degradation phenomena. In the past years, the Light Water Reactor Sustainability (LWRS) program has investigated Radiation-Induced Volumetric Expansion (RIVE) as a potential degradation mechanism for concrete biological shields [Graves et al., 2014, Rosseel et al., 2016]. RIVE causes swelling and micro-mechanical damage in concrete due to the amorphization of mineral phases contained in the aggregates under neutron irradiation [Hilsdorf et al., 1978, Rosseel et al., 2016]. For long-term operations, it is critical to assess the durability of concrete after 60 or 80 years of exposure to NPP operating conditions against this phenomenon.

RIVE is dependent on the composition of the aggregates used in concrete. Quartz-bearing aggregates are more sensitive to RIVE than calcite-bearing aggregates, for example. However, the aggregate composition of a specific plant is generally not explicitly given in the concrete formulation, which makes it nearly impossible to predict the resistance of that concrete to RIVE. Additional characterization is needed to identify the radiation-sensitive mineral phases contained in the aggregates.

Therefore, in order to assess the sensitivity of a specific concrete to neutron irradiation, one must rely on a rigorous combination of:

- An analysis of the phases present in the concrete. The LWRS program acquired a micro-X-Ray Fluorescence (μ-XRF) unit for that purpose (LWRS reports M3LW-17OR0403013 and M2LW-17OR0403014).

- Appropriate models and material parameters for each of the phases identified. The IMAC database was established to compile data for minerals, aggregates and concrete exposed to irradiation and validate models using that data (LWRS reports M2LW-17OR403044 and M3LW-17OR0403045).

- Physics-based upscaling methods able to account for the complex behavior of the concrete (LWRS report M3LW-15OR0403044).

This report specifically addresses the third point, and demonstrates new capabilities. In previous work, upscaling was done using a Finite Element Method (FEM) model validated against data from the literature. However, that model suffered from two strong limitations:

- It cannot handle complex geometrical shapes, as it was developed with spheres and simple polygons.

- It is highly computationally intensive, making it impossible to use on high-resolution microstructures such as those extracted from μ-XRF spectra.

For these reasons, different upscaling methods are being investigated.

In recent years, Fast Fourier Transform (FFT) methods have been developed as an alternative to FEM. They have notably been applied to thermo-elastic properties, plasticity of polycrystalline alloys, and concrete creep [Moulinec and Suquet, 1998, Liu et al., 2010, Lavergne et al., 2015]. It is able to handle much larger problems than FEM, and thus can be applied to simulate microstructures obtained from μ-XRF or similar microstructural characterization techniques (see Figure 1).

In the present work, FFT solvers from the literature are implemented and validated for 2-dimensional concrete microstructures. The solvers are able to characterize elastic strain and stress fields in a material subject to an imposed strain or stress, as well as internal strains such as thermal expansion or RIVE. An example of simulation using a microstructure characterized with μ-XRF is provided to demonstrate the capabilities of the solver to simulate large concrete microstructures.

FEM

FFT

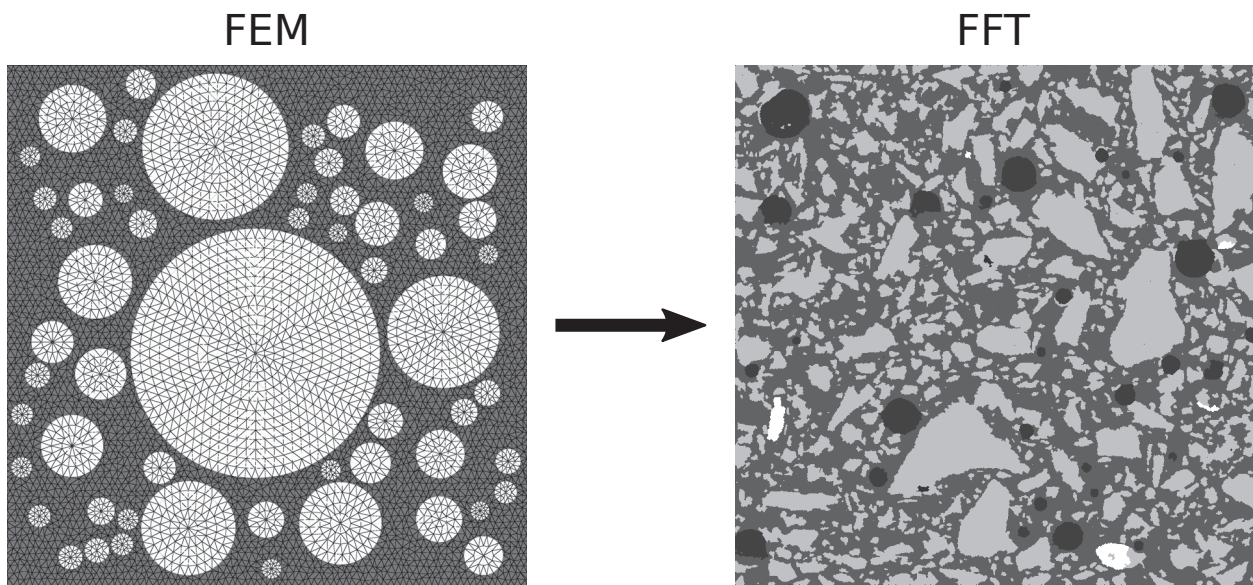**Figure 1. Example of concrete microstructures simulated with FEM (left, figure from [Giorla et al., 2015], ≈12,000 elements, 2 phases: cement, aggregates) and with FFT (present report, 640,000 pixels, 4 phases: porosity, cement, calcite, ankerite).**

INTRODUCTION

In the United States, NPPs are being evaluated for a second license renewal, extending their service life from 60 to 80 years. Doing so requires the assessment of the durability of all components under long-term operating conditions. This includes the concrete used for the NPP structure, notably the Concrete Biological Shield (CBS), which is exposed to a particularly high neutron and gamma dose, and which may, for some LWRS, exceed the threshold at which degradation has been reported in the literature [Esselman and Bruck, 2013, Graves et al., 2014, Rosseel et al., 2016].

Concrete exposed to neutron irradiation is subject to a very high volumetric expansion and a loss of engineering properties (notably elastic stiffness, strength) [Hilsdorf et al., 1978, Field et al., 2015]. This is predominantly driven by the Radiation-Induced Volumetric Expansion (RIVE) of the minerals that compose the concrete aggregates [Rosseel et al., 2016]. The swelling of these minerals under neutron irradiation places the cement paste under very high stresses. This ultimately leads to micro-cracking in the cement paste [Le Pape et al., 2015, Giorla, 2015, Giorla et al., 2015], which manifests as a loss of mechanical properties of the concrete.

This process is highly dependent on the nature of the minerals contained in the aggregates. For example, quartz (a silicate) is highly sensitive to RIVE, while the effects on calcite (a carbonate) are comparatively much lower. Furthermore, most aggregates are heterogeneous, with varied and complex microstructures. This may lead to internal cracking inside the aggregates before cracking propagates through the cement paste. This effect depends on the microstructure of the aggregates themselves, and the geometrical arrangement of mineral phases with respect to one another.

Therefore, it is not possible to estimate sensitivity of a given concrete to RIVE without the characterization of its mineral composition and microstructure. It is also generally not possible to perform accelerated irradiation tests due to the very high cost associated with radiation experiments. The sensitivity of a given material to RIVE must then be evaluated through the rigorous combination of:

- An analysis of the phases present in the concrete, including their nature and their geometrical arrangement. Last year, the LWRS program acquired a μ-XRF instrument to analyze the phases contained in a specimen [Tajuelo Rodriguez, 2017]. The instrument provides two-dimensional elemental concentration maps of materials, with a maximum area of 4×4 cm, and a resolution of 10 μm. In a previous work, a methodology to identify mineral phases from μ-XRF maps was developed [Giorla, 2017].

- Appropriate models and material parameters for each of the phases identified when exposed to neutron irradiation. The LWRS program has compiled a set of data on the irradiation properties of minerals and aggregates in the IMAC database [Le Pape, 2016, 2017]. In the present work, the data on minerals is of interest. It contains information on the non-irradiated properties of each mineral (notably, the elastic constants), as well as irradiated properties experimentally determined by other researchers (notably, the volumetric expansion). The database is associated with semi-empirical models allowing researchers the ability to derive the RIVE of a specific mineral as a function of both the neutron fluence and the temperature.

- Physics-based upscaling methods able to account for the complex behavior of the concrete. In a previous work, a FEM-based model was developed to upscale the RIVE of aggregates to the concrete scale, accounting for the creep-damage interaction inside the cement paste [Giorla, 2015]. The model was validated against experimental data from the literature [Giorla et al., 2015], and used to assess coupled temperature-irradiation effects [Le Pape et al., 2016].

However, the FEM model has two strong limitations which makes it not applicable for the analysis of microstructures obtained through μ-XRF.

- It is not able to handle the complex geometries acquired by the μ-XRF. Indeed, the FEM model was designed to incorporate simple shapes of inclusions (such as circles and polygons), and was not developped to handle high-resolution images.

- The computational time to simulate large-scale microstructures would be prohibitive to use in practice due to the complexity of the creep-damage algorithm.

For these reasons, other upscaling approaches need to be investigated.

Fast Fourier Transform (FFT) is a numerical technique that has emerged at the mid 90's to evaluate homogeneous properties of periodic microstructures [Moulinec and Suquet, 1994]. Since its initial formulation for elastic materials, it has been extended to account for plasticity [Moulinec and Suquet, 1998], linear visco-elasticity [Lavergne et al., 2015] and finite strains [Kabel et al., 2014]. Furthermore, new solvers have been formulated to improve their convergence properties, notably for the case of materials with high contrast [Eyre and Milton, 1999, Brisard and Dormieux, 2010, Zeman et al., 2010, Moulinec and Silva, 2014]. The main strength of FFT solvers is their ability to handle very large microstructures thanks to their low memory cost, which makes this method ideal for the analysis of μ-XRF maps, and therefore, the analysis of RIVE in concrete.

In this report, the FFT method is presented first. Two different algorithms from the literature are shown. Both algorithms can compute the properties of elastic materials with imposed eigenstrains (such as the thermal expansion or RIVE).

Second, applications are presented. Analytical results are reproduced to demonstrate the correct implementation of the method. Then, an example using a microstructure analyzed by μ-XRF is presented, using data from the IMAC database.

The conclusion discusses the avenues these FFT solvers open, and the future developments required to simulate RIVE-induced damage.

FAST FOURIER TRANSFORM

The Fast Fourier Transform method is a numerical method to compute the stresses and strains in periodic heterogeneous materials. It has been developed since the mid 90's [Moulinec and Suquet, 1994, 1998] in order to alleviate the limitations of the FEM for the simulation of complex microstructures.

The FFT computes the strains and stresses in a periodic, heterogeneous material subject to a uniform macroscopic stress or strain. It applies to a unit cell of the material microstructure, and is valid in both 2- and 3-dimensions.

THEORY - ELASTICITY

We consider a 2- or 3-dimensional spatial domain representing the unit cell of a periodic heterogeneous material. $\mathbf{x}$ denotes the vector of coordinates in that domain, and L_i the dimension of the unit cell in the ith direction. At each point, the material constitutive behavior is governed by linear elasticity:

$$\sigma(\mathbf{x}) = \mathbb{C}(\mathbf{x}) : \left(\epsilon(\mathbf{x}) - \epsilon_{imp}(\mathbf{x}) \right) \tag{1}$$

With σ the stress, ϵ the strain, ϵ_{imp} the eigenstrain (self-induced strains which cause no stress, such as thermal expansion), and $\mathbb{C}$ the stiffness tensor of the material at that point.

FFT methods require $\mathbb{C}(\mathbf{x}) \neq \mathbf{0} \forall \mathbf{x}$. Therefore, porosity or cracks need to be attributed a small (non-zero) stiffness to be simulated.

The material is subject to a macroscopic strain $\mathbf{E}$ (the case of an imposed macroscopic stress is discussed in a later section). Under these conditions, the resulting displacement field is also periodic with the same periodicity as the material property. It is sufficient to calculate its fluctuations on the unit cell to obtain the overall properties of the material.

The FFT method considers these fluctuations using a so-called reference material, with an homogeneous stiffness of $\mathbb{C}_0$ [Moulinec and Suquet, 1998]. The stress polarization field τ is introduced as a measure of the stress fluctuations in the material:

$$\tau(\mathbf{x}) = (\mathbb{C}(\mathbf{x}) - \mathbb{C}_0) : \epsilon(\mathbf{x}) \tag{2}$$

The solution of the micro-mechanical problem then obeys [Kröner, 1977]:

$$\epsilon(\mathbf{x}) = \mathbf{E} - (\Gamma_0 * \tau)(\mathbf{x}) \tag{3}$$

With Γ_0 the fourth-order Green tensor associated with the reference material, and $*$ the convolution product operator. This convolution product is conveniently evaluated in the Fourier space:

$$\hat{\epsilon}(\boldsymbol{\xi}) = \begin{cases} -\hat{\Gamma}_0(\boldsymbol{\xi}) : \hat{\tau}(\boldsymbol{\xi}) & (\boldsymbol{\xi} \neq \mathbf{0}) \\ \mathbf{E} & (\boldsymbol{\xi} = \mathbf{0}) \end{cases} \tag{4}$$

With $\hat{}$ the Fourier transform of a given variable, and $\boldsymbol{\xi}$ the frequencies in the Fourier space. The Fourier transform of an integrable (real) function f is an integrable (complex) function $\hat{f}$ given by:

$$\hat{f}(\boldsymbol{\xi}) = \int\limits_{-\infty}^{\infty} f(\mathbf{x})\, e^{-2\pi i \mathbf{x} \boldsymbol{\xi}} d\mathbf{x} \tag{5}$$

(5) can be evaluated numerically by assuming that f is step-wise constant with the Fast Fourier Transform method.

The numerical advantage of the formulation (4) is that the convolution can be evaluated localy in the Fourier space (it only depends on the variables at a given frequency) as opposed to globally in the real space. The numerical difficulty becomes the Fourier transform of the strain and polarization fields, and its inverse. In the present work, this is carried out using the FFTW library [Frigo and Johnson, 2005], which is commonly used in FFT packages for micromechanics.

Assuming the reference material is isotropic, the transformed Green operator $\hat{\Gamma}_0$ is given by [Moulinec and Suquet, 1998]:

$$\hat{\Gamma}_{0,ijkl}(\boldsymbol{\xi}) = \frac{1}{4\mu_0 \|\boldsymbol{\xi}\|^2} \left(\delta_{ki}\xi_l\xi_j + \delta_{lj}\xi_k\xi_i + \delta_{li}\xi_k\xi_j + \delta_{kj}\xi_l\xi_i \right) - \frac{\lambda_0 + \mu_0}{\mu_0 (\lambda_0 + 2\mu_0)} \frac{\xi_i\xi_j\xi_k\xi_l}{\|\boldsymbol{\xi}\|^4} \tag{6}$$

With λ_0 and μ_0 the first Lamé parameter and the shear modulus of the reference material, and $\|.\|$ the Euclidian norm. One can verify that this formulation has the same symmetries as a fourth-order stiffness tensor. However, it is not isotropic.

$\hat{\Gamma}$ is not defined for $\boldsymbol{\xi} = \mathbf{0}$, which is why $\hat{\epsilon}(\mathbf{0})$ is set to $\mathbf{E}$.

Furthermore, transforming $\hat{\epsilon}$ back to the real space ϵ requires $\hat{\epsilon}(-\boldsymbol{\xi})$ to be equal to the conjugate of $\hat{\epsilon}(\boldsymbol{\xi})$. The implementation of the FFTW library naturally enforces this condition, except for some of the highest frequencies. [1] In this case, the approach recommended in [Moulinec and Suquet, 1998] is to force the stress at these frequencies to be equal to the macroscopic stress. This can be achieved by replacing $\hat{\Gamma}_0$ with $\mathbb{C}_0^{-1}$ for these frequencies.

BASIC ALGORITHM

The basic algorithm presented in [Moulinec and Suquet, 1994, 1998] solves (3) using a fixed-point iterative procedure. The strength of the algorithm is that the convolution product is evaluated in the Fourier space, while the polarization field is evaluated in the real space, allowing both operations to be executed locally instead of globally.

The algorithm can be written as follow:

---

[1]For a 2-dimensional domain, this happens when the number of pixels in the first direction is even. For a 3-dimensional domain, this happens when the number of pixels in the first or second directions are even.

Algorithm 1 Basic FFT scheme

Material properties $\mathbb{C}(\mathbf{x})$, $\epsilon_{imp}(\mathbf{x})$, and $\hat{\Gamma}_0(\xi)$ are provided
Initial strain field $\epsilon^0(\mathbf{x})$ is provided
$\hat{\epsilon}^0 = \mathbf{FFT}(\epsilon^0)$
while not *converged* **do**
   for each $\mathbf{x}$ **do**
     $\sigma^n(\mathbf{x}) = \mathbb{C}(\mathbf{x}) : \left(\epsilon^n(\mathbf{x}) - \epsilon_{imp}(\mathbf{x}) \right)$
   end for
   $\hat{\sigma}^n = \mathbf{FFT}(\sigma^n)$
   for each $\xi \neq \mathbf{0}$ **do**
     $\hat{\epsilon}^{n+1}(\xi) = \hat{\epsilon}^n(\xi) - \hat{\Gamma}_0(\xi) : \hat{\sigma}^n(\xi)$
   end for
   $\hat{\epsilon}^{n+1}(\mathbf{0}) = \mathbf{E}^{n+1}$
   $\epsilon^{n+1} = \mathbf{FFT}^{-1}(\hat{\epsilon}^{n+1})$
end while

$\mathbf{E}^{n+1}$ is the prescribed macroscopic strain at the $(n + 1)^{\text{th}}$ iteration. When the material is subject to a macroscopic strain $\mathbf{E}$, then $\mathbf{E}^{n+1} = \mathbf{E}$. For a material subject to a macroscopic stress, $\mathbf{E}^{n+1}$ must be adjusted at each iteration (see below).

Convergence is achieved when the error reaches a user-specified criterion. For FFT schemes, the error $\mathcal{E}$ can be decomposed into three different components: error on equilibrium $\mathcal{E}_{eq}$, the error on the boundary conditions $\mathcal{E}_{bc}$ and the strain compatibility error $\mathcal{E}_{comp}$:

$$\mathcal{E}^n = \max\left(\frac{\mathcal{E}_{eq}^n}{\mathcal{E}_{eq}^0}, \frac{\mathcal{E}_{bc}^n}{\mathcal{E}_{bc}^0}, \frac{\mathcal{E}_{comp}^n}{\mathcal{E}_{comp}^0} \right) \tag{7}$$

The equilibrium error is a measure of the divergence of the stress field in the sample. According to classical solid continuum mechanics, this divergence must be equal to 0. It is evaluated locally in the Fourier space with:

$$\mathcal{E}_{eq}^n = \frac{\sqrt{\sum_{\xi} \| \xi . \hat{\sigma}^n(\xi) \|^2}}{\| \hat{\sigma}^n(\mathbf{0}) \|} \tag{8}$$

The error on the boundary condition reads, for a prescribed macroscopic strain $\mathbf{E}$:

$$\mathcal{E}_{bc}^n = \frac{\| < \epsilon^n(\mathbf{x}) > - \mathbf{E} \|}{\| \mathbf{E} \|} \tag{9}$$

Where $< . >$ denotes the spatial average.

The error on the compatibility derives from the kinematic compatibility of the strain field. It can be computed in the Fourier space using (in 2 dimensions):

$$\mathcal{E}_{comp}^n = \frac{\max\left(\left\| 2\xi_1 \xi_2 \hat{\epsilon}_{12}^n(\xi) - \xi_2 \xi_2 \hat{\epsilon}_{11}^n(\xi) - \xi_1 \xi_1 \hat{\epsilon}_{22}^n(\xi) \right\| \right)}{\sqrt{\sum_{\xi} \hat{\epsilon}_{ij}^n(\xi) : \text{conj}\left(\hat{\epsilon}_{ij}^n(\xi) \right)}} \tag{10}$$

Extensions to 3 dimensions can be found in [Moulinec and Silva, 2014].

This scheme converges on the following conditions [Michel et al., 2001]:

$$\mu_0 > \frac{\mu(\mathbf{x})}{2} \quad , \quad \lambda_0 > \frac{\lambda(\mathbf{x})}{2} \tag{11}$$

This algorithm ensures that, at each step, both $\mathcal{E}_{bc}$ and $\mathcal{E}_{comp}$ are equal to 0.

ACCELERATED ALGORITHM

The accelerated algorithm represents a class of similar algorithms designed to improve the convergence properties of the basic algorithm presented above. The first versions of these algorithms were given by Eyre and Milton [1999] and Michel et al. [2000], before Monchiet and Bonnet [2012] showed the more general case.

The original algorithm did not account for additional eigenstrain. In the present work, the algorithm of [Monchiet and Bonnet, 2012] is extended to be able to simulate elastic materials with eigenstrains, following the work of [Lavergne et al., 2015] for viscoelasticity.

The scheme is controlled by two numerical parameters α and β which can be controlled by the user. As noted by Moulinec and Silva [2014], the algorithm of Eyre and Milton [1999] corresponds to $\alpha = \beta = 2$, while the algorithm of Michel et al. [2000] corresponds to $\alpha = \beta = 1$.

The accelerated algorithm can be written as follow:

Algorithm 2 Accelerated FFT scheme

Parameters α and β are provided
Material properties $\mathbb{C}(\mathbf{x})$, $\epsilon_{imp}(\mathbf{x})$, and $\hat{\Gamma}_0(\boldsymbol{\xi})$ are provided
Initial strain field $\epsilon^0(\mathbf{x})$ is provided
while not *converged* **do**
  for each $\mathbf{x}$ **do**
    $\tau_\alpha^n(\mathbf{x}) = \mathbb{C}(\mathbf{x}) : \epsilon^n(\mathbf{x}) + (1 - \beta)\,\mathbb{C}_0 : \epsilon^n(\mathbf{x})$
    $\tau_\beta^n(\mathbf{x}) = \alpha\,\mathbb{C}(\mathbf{x}) : \left(\epsilon^n(\mathbf{x}) - \epsilon_{imp}(\mathbf{x})\right) - \beta\,\mathbb{C}_0 : \epsilon^n(\mathbf{x})$
  end for
  $\hat{\tau}_\beta^n = \mathbf{FFT}(\tau_\beta^n)$
  for each $\boldsymbol{\xi} \neq \mathbf{0}$ **do**
    $\hat{\epsilon}_\beta^{n+1}(\boldsymbol{\xi}) = -\hat{\Gamma}_0(\boldsymbol{\xi}) : \hat{\tau}_\beta^n(\boldsymbol{\xi})$
  end for
  $\hat{\epsilon}_\beta^{n+1}(\mathbf{0}) = \beta\,\mathbf{E}^{n+1}$
  $\epsilon_\beta^{n+1} = \mathbf{FFT}^{-1}(\hat{\epsilon}_\beta^{n+1})$
  for each $\mathbf{x}$ **do**
    $\epsilon^{n+1}(\mathbf{x}) = (\mathbb{C}(\mathbf{x}) + \mathbb{C}_0)^{-1} : \left(\tau_\alpha^n(\mathbf{x}) + \mathbb{C}_0 : \epsilon_\beta^{n+1}(\mathbf{x})\right)$
    $\sigma^{n+1}(\mathbf{x}) = \mathbb{C}(\mathbf{x}) : \left(\epsilon^{n+1}(\mathbf{x}) - \epsilon_{imp}(\mathbf{x})\right)$
  end for
end while

For performance reasons, $(\mathbb{C}(\mathbf{x}) + \mathbb{C}_0)^{-1}$ should be evaluated before the main iteration loop.

The convergence criterion are the same as described for the basic algorithm. However, this scheme does not ensure the compatibility of the strain or the boundary conditions at each step of the algorithm, meaning that $\mathcal{E}_{bc}$ and $\mathcal{E}_{comp}$ must be calculated.

As proved by Moulinec and Silva [2014], these schemes are convergent under the following conditions:

$$0 \leq \alpha < 2, \ 0 \leq \beta < 2, \lambda_0 > 0, \mu_0 > 0 \tag{12}$$

Eyre and Milton [1999] also showed that the scheme is convergent for $\alpha = \beta = 2$.

IMPOSING A MACROSCOPIC STRESS

In certain cases, it might be more appropriate to impose a macroscopic stress Σ rather than a macroscopic strain $\mathbf{E}$ (for example, to simulate a creep test or a stress-free expansion test). The algorithms presented above can still be used for these cases, except that the macroscopic strain applied must be adjusted at each iteration of the solver. The updated macrostrain $\mathbf{E}^n$ is given by [Lavergne et al., 2015]:

$$\mathbf{E}^n = \mathbb{C}_0 : (\Sigma - < \sigma^n >) + < \epsilon^n > \tag{13}$$

The error on the boundary conditions is calculated as:

$$\mathcal{E}_{bc}^n = \frac{\| < \sigma^n(\mathbf{x}) > - \Sigma \|}{\| \Sigma \|} \tag{14}$$

CHOICE OF REFERENCE MEDIUM

The convergence properties of the FFT algorithms depend on both the contrast between the mechanical properties of the different phases, and the choice of reference medium (see [Moulinec and Silva, 2014] for a complete convergence analysis).

For the FFT basic scheme, the reference medium can be chosen as:

$$\mu_0 = \frac{\mu_{min} + \mu_{max}}{2} \quad , \quad \lambda_0 = \frac{\lambda_{min} \lambda_{max}}{2} \tag{15}$$

Notably, the reference medium that maximizes the convergence rate when of the FFT accelerated scheme when $\alpha = \beta$ is given by:

$$\mu_0 = \sqrt{\mu_{min} \mu_{max}} \quad , \quad \lambda_0 = \sqrt{\lambda_{min} \lambda_{max}} \tag{16}$$

VALIDATION

Each solver is validated on a basic numerical test to check their correct implementation.

The test consists of a 32×32 pixel domain representing a layered bi-phasic material. The material properties of each material and the reference material are presented in Table 1. The microstructure is shown in Figure 2. For these simulations, the materials have no eigenstrains ($\epsilon_{imp}(\mathbf{x}) = \mathbf{0}$), unless specified otherwise.

7

Three loading scenarios are investigated:

- An imposed shear strain $\mathbf{E} = \{0, 0, 0.001\}$. In this case, the resulting stress should be uniform in the whole material while the resulting strain should be uniform per phase.

- An imposed axial stress $\mathbf{\Sigma} = \{0, 1 \times 10^6, 0\}$. In this case, the resulting strain should be uniform in the whole material, while the resulting stress should be uniform per phase.

- Both materials have an eigenstrain of $\epsilon_{imp}(\mathbf{x}) = \{0.001, 0.001, 0\}$, and the material is set free ($\mathbf{\Sigma} = \mathbf{0}$). In this case, both the resulting strain and stress fields should be uniform in the whole material, and the stress field should be equal to 0.

Results are gathered in Table 2. The error on the strain $\mathcal{E}_\epsilon$ and on the stress $\mathcal{E}_\sigma$ are calculated as:

$$\mathcal{E}_\epsilon = \max_{\mathbf{x}} \left(\frac{\left\| \epsilon(\mathbf{x}) - \epsilon_{analytic}(\mathbf{x}) \right\|}{\mathbf{E}} \right), \ \mathcal{E}_\sigma = \max_{\mathbf{x}} \left(\frac{\left\| \sigma(\mathbf{x}) - \sigma_{analytic}(\mathbf{x}) \right\|}{\mathbf{\Sigma}} \right) \tag{17}$$

The solvers are set with a convergence criterion of 1×10^{-7}.

Table 1. Material properties used for the validation of the FFT solvers.

	E [GPa]	ν [−]	λ [GPa]	μ [GPa]
Material 1	10	0.2	2.77777	4.16666
Material 2	20	0.2	5.55555	8.33333
Reference material	15	0.2	4.16666	6.25

Table 2. Solver validation.

Solver	Test case	Iterations at convergence	$\mathcal{E}$	$\mathcal{E}_\epsilon$	$\mathcal{E}_\sigma$
FFTFixedPointSolver	Shear strain	1	1.30104×10^{-11}	1.30104×10^{-13}	2.12900×10^{-14}
	Axial stress	16	2.33684×10^{-8}	4.03308×10^{-8}	1.61323×10^{-8}
	Eigenstrain	1	1.21385×10^{-10}	4.33680×10^{-15}	1.14443×10^{-7}
FFTPolarizationSolver	Shear strain	10	2.14196×10^{-8}	1.73472×10^{-15}	2.37996×10^{-9}
	Axial stress	11	3.01226×10^{-8}	1.73387×10^{-8}	4.50661×10^{-9}
	Eigenstrain	1	1.08608×10^{-10}	4.33680×10^{-15}	1.02396×10^{-7}

Figure 2. Layered microstructure for solver validation (material 1 in black, material 2 in grey).

IMPLEMENTATION

These algorithms are implemented in the Microstructure-Oriented Scientific Analysis of Irradiated Concrete (MOSAIC) software package currently in development at ORNL, and which was used in an earlier work to analyze μ-XRF [Giorla, 2017]. MOSAIC is implemented in C++ and maintained under ORNL internal Github repository.

MOSAIC stores data and numerical algorithms in the following classes:

- A `Field` object stores the numerical value of a field on a regular grid.

  - It can represent a scalar field (such as temperature, or concentration), a vector field (such as stress or strain in Voigt notation), a matrix field (such as a stiffness matrix in Voigt notation), a fourth-order tensor field (such as a full fourth-order stiffness tensor), or any multi-dimensional array. Methods are provided to extract specific components of a field (for example, to extract the ϵ_{11} strain component).

  - The values are stored on a regular grid, which itself can be multi-dimensional (an image would be a 2-dimensional grid, while the output of a X-Ray Computed Tomography (CT) scan would be a 3-dimensional grid), and of arbitrary dimensions.

  - Fields can be pure real, or complex (containing both a real and imaginary parts).

- A series of `Operation` classes, that represent functions applied to `Field` objects.

  - An `Operation` takes into input a number of `Field` objects (including none), and have a single `Field` output. From an algorithmic perspective, each statement in the FFT algorithms presented above is a separate `Operation`.

  - An `Operation` can be global (for example, the Fast Fourier Transform itself), or pixel-wise (that is, the same function is applied at each pixel; for example, all the matrix-vector operations in the

9

FFT algorithms). In the later case, the `Operation` is run in parallel in a thread-safe environment.
[2]

– A series of checks ensures that an `Operation` is run on `Field` objects of appropriate dimensions and types. If not, or if an error occurs during its execution, then an error message is thrown to the main program and displayed to the user.

- A series of `IterativeSolver` classes, that compute a solution to a numerical problem. The FFT algorithms presented above are each `IterativeSolver`-type classes.

  – An `IterativeSolver` stores the data necessary for its execution. Mechanical solvers, for example, store the stress and strain fields, as well as the stiffness and eigenstrain fields. FFT solvers also store the Fourier transform of the strain and stress fields, and other intermediate variables required.

  – Each `IterativeSolver` contains a series of `Operation` that are applied at each iteration. These `Operation` objects represent each statement in the FFT algorithms presented above.

  – An `IterativeSolver` also defines the convergence criterion used to stop the algorithm. The user can also specify a maximum number of iterations to avoid an infinite simulation.

  – The basic FFT scheme is implemented as a `FFTFixedPointSolver`, and the accelerated FFT scheme is implemented as the `FFTPolarizationSolver`.

MOSAIC uses XML files to export/import data. This notably allows MOSAIC to read data from the IMAC database.

While MOSAIC architecture has been designed for both 2- and 3-dimensional simulations, the Green operator and the FFT solvers have only been implemented and validated in 2D at this stage.

---

[2]The system ensures that one thread cannot read the value of a certain pixel while another is modifying it.

EXAMPLES

The FFT solvers are applied to simulate a piece of concrete analyzed by μ-XRF. The analysis of the specimen was performed using MOSAIC in [Giorla, 2017].

The simulations in this section are shown as a proof of concept for the application of FFT solvers for the analysis of concrete exposed to RIVE.

The microstructure is discretized on a grid of 800×800 pixels, with a resolution of $10\ \mu m$. Four phases were identified:

- Porosity

- Cement paste

- Calcite ($CaCO_3$)

- Ankerite ($Ca(Fe, Mg, Mn)(CO_3)_2$)

The analysis also provided boundaries between particles as a separate phase. Since the FFT method assumes perfect interface between grains, the pixels identified as boundaries are attributed to the most prevalent neighboring phase. The result of the phase analysis is shown in Figure 3.

The mechanical properties of each phases are reported in Table 3. Since FFT methods cannot simulate materials with a zero stiffness, porosity is attributed a small Young's modulus, arbitrarily taken as 0.1 GPa in a first approximation. The influence of the choice of this modulus is examined later in this section.

The properties of calcite and ankerite are taken from the IMAC database [Le Pape, 2016]. Both calcite and ankerite are anisotropic materials (ankerite has a trigonal crystal symmetry, while calcite has a trigonal crystal symmetry). Given that the simulations are two-dimensional, it is necessary to transform the full stiffness tensor of these materials (21 independent components) into a two-dimensional tensor (6 independent components). For these preliminary simulations, the stiffness tensors of ankerite and calcite are transformed using the following rules, so that they become isotropic:

$$\mathbb{C}^{2D}_{1111} = \mathbb{C}^{2D}_{2222} = \frac{1}{3}\left(\mathbb{C}^{3D}_{1111} + \mathbb{C}^{3D}_{2222} + \mathbb{C}^{3D}_{3333}\right) \tag{18}$$

$$\mathbb{C}^{2D}_{1122} = \frac{1}{3}\left(\mathbb{C}^{3D}_{1122} + \mathbb{C}^{3D}_{1133} + \mathbb{C}^{3D}_{2233}\right) \tag{19}$$

$$\mathbb{C}^{2D}_{1112} = \mathbb{C}^{2D}_{2212} = 0 \tag{20}$$

$$\mathbb{C}^{2D}_{1212} = \frac{1}{2}\left(\mathbb{C}^{2D}_{1111} - \mathbb{C}^{2D}_{1122}\right) \tag{21}$$

This is a crude approximation for the purpose of demonstrating the solver's capabilities. It would be more accurate to project $\mathbb{C}$ according to the orientation of each crystal, but this would require further characterization on the same sample. An example of anisotropic simulation is provided later in this section to showcase the ability of the FFT method to simulate anisotropic minerals.
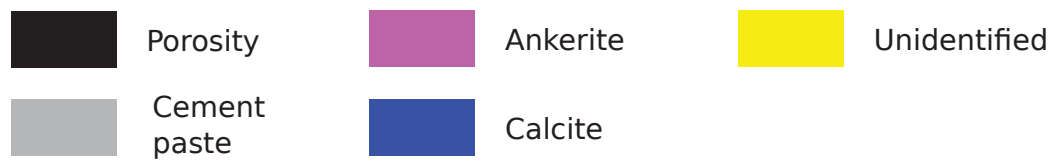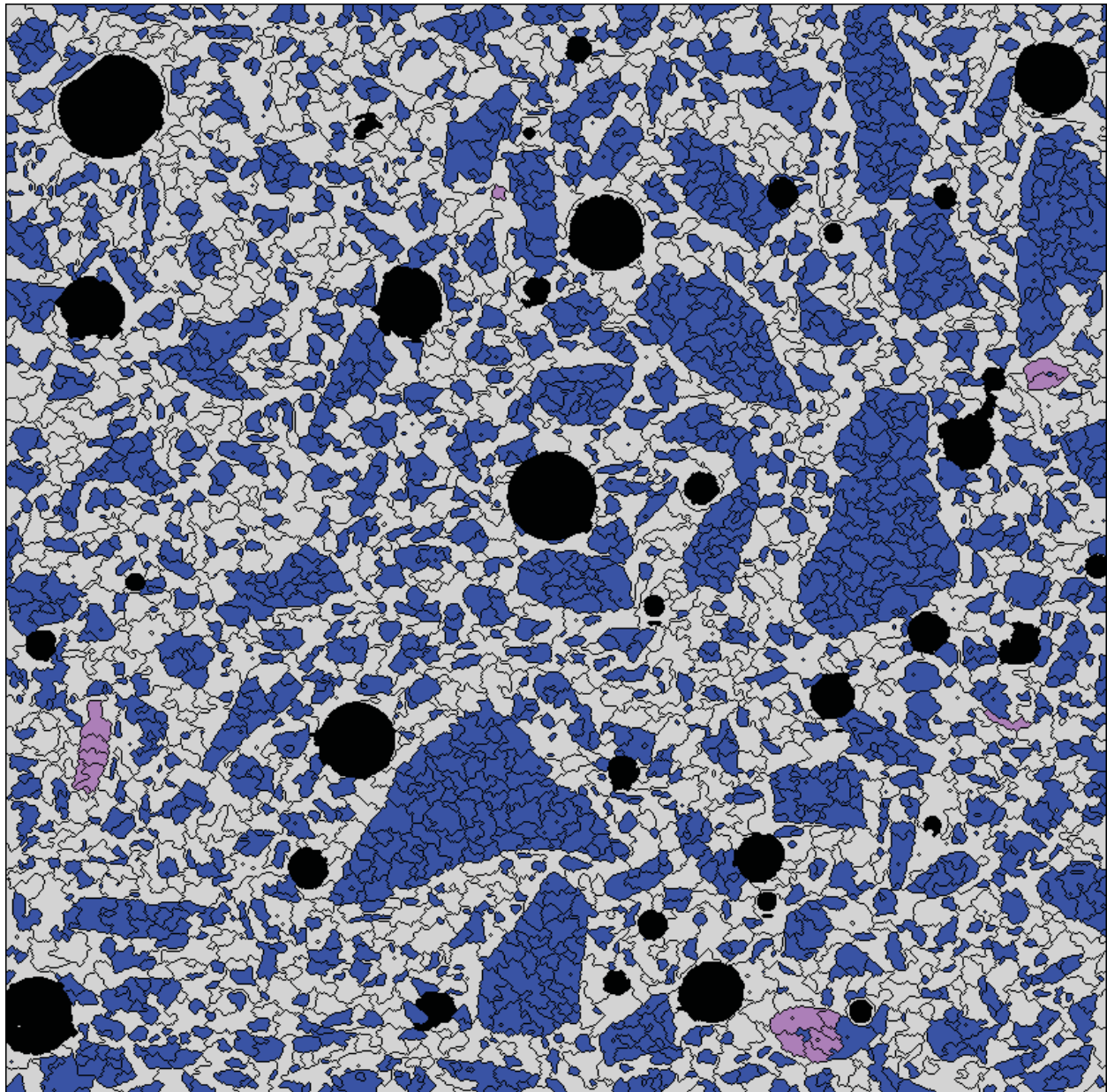
Figure 3. Phase analysis of the concrete specimen. Figure taken from [Giorla, 2017].

AXIAL TENSION TESTS

First, two simple elastic tests are performed. The first test is an imposed axial strain test $\mathbf{E} = \{0.001, 0, 0\}$. The second test is an imposed axial stress test $\mathbf{\Sigma} = \{1 \times 10^6, 0, 0\}$. The basic (`FFTFixedPoint`) and accelerated solver (`FFTPolarization`, with $\alpha = \beta = 2$) are used and their solutions compared, with an error tolerance of 1×10^{-6}.

Tables 4-5 compare the results of both solvers in terms of average, minimum and maximum strains and stresses. Both solvers provide identical results to the machine precision. Notably, one can verify that in all cases, the imposed strain (or stress) are accurately calculated.

Figure 4 shows the distribution of stresses and strains in the microstructure. Very high values of strains can be found at the boundary between the porosity and the cement paste, notably in areas with geometrical defects. High values of stresses are generally located at the boundary between cement paste and either aggregates or porosity, notably in places where two aggregates are very close to one another.

Table 6 compares both solvers in term of their convergence properties: number of iterations required to reach convergence, and computational time (measured on a Linux workstation with 6 threads).

The number of iterations for the accelerated scheme is significantly lower than for the basic scheme, but the computational time for each iteration is also higher. This is partly due to the fact that the calculation of $\mathcal{E}_{eq}$ and $\mathcal{E}_{comp}$ for the accelerated scheme requires the evaluation of $\mathbf{FFT}(\epsilon)$ and $\mathbf{FFT}(\sigma)$ respectively, which are not evaluated during the main solver iteration (as opposed to the basic solver). Therefore, and following the approach used by Lavergne et al. [2015], these are evaluated only every n iterations, where n is a user-defined parameter (for the following, $n = 5$). Doing so reduces the computational time for each iteration from 0.26 s to 0.17 s.

A comparison of the error as a function of the number of iterations is shown in Figure 5.

Table 3. Mechanical properties of all phases

Phase	λ [GPa]	μ [GPa]	Surface fraction [%]
Porosity	0.0277	0.0416	3.55
Cement paste	3.3333	5	34.68
Calcite	53.6571	36.0262	61.44
Ankerite	61.9333	56.4666	0.32
Reference material (`FFTFixedPoint`)	30.9805	28.2541	
Reference material (`FFTPolarization`)	1.3116	1.5338	

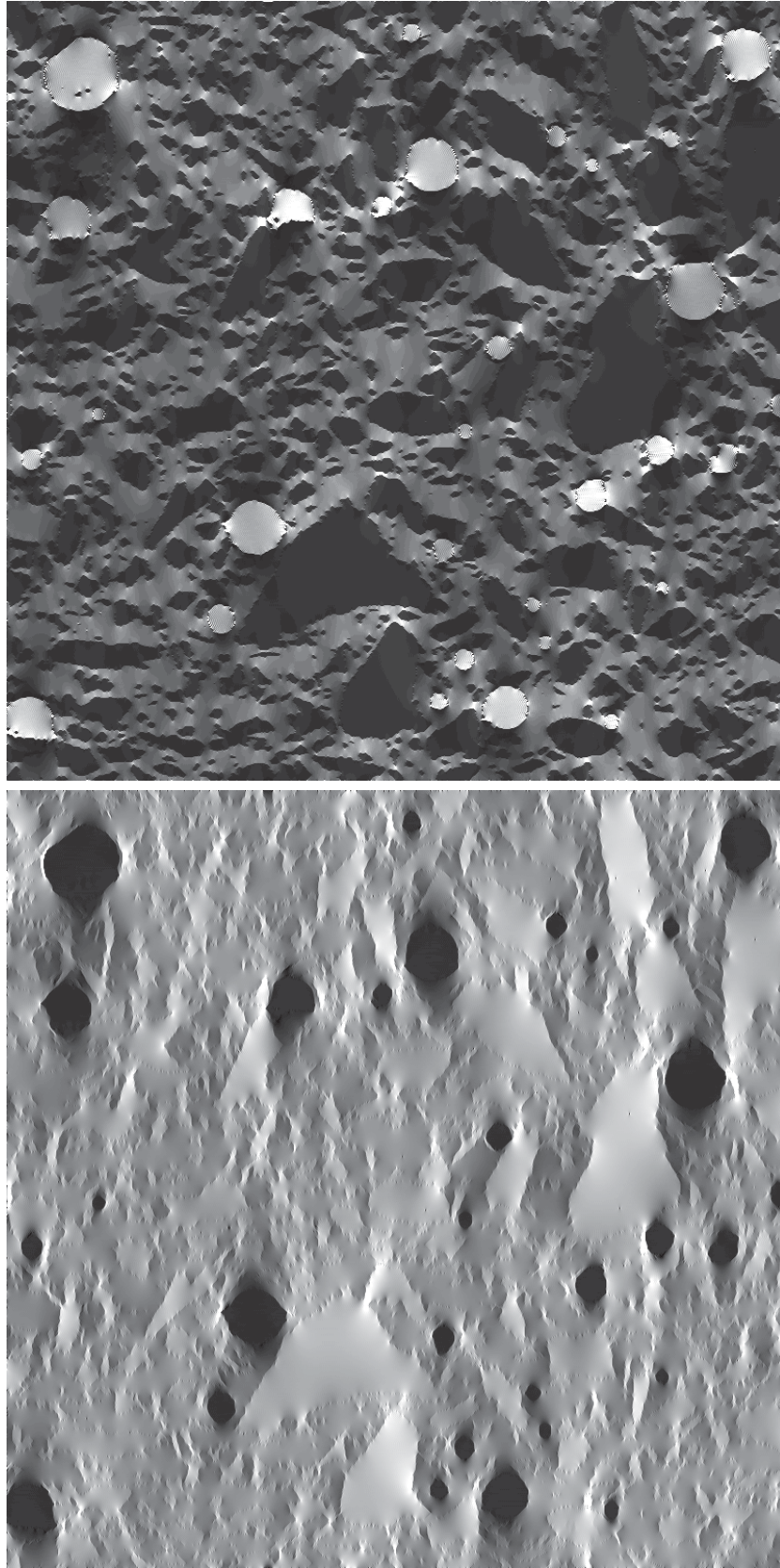**Figure 4.** ϵ_{11} (top) and σ_{11} (bottom) components of the strain and stress fields for the concrete sample subject to an imposed axial strain. High values are in white, low values in black.

Table 4. Solver comparison (stress and strain) for the imposed strain test

Value	Minimum		Average		Maximum	
	FixedPoint	Polarization	FixedPoint	Polarization	FixedPoint	Polarization
ϵ_{11} [−]	-0.0118	-0.0118	0.001	0.001	0.0388	0.0388
ϵ_{22} [−]	-0.0146	-0.0146	-5.9×10^{-23}	-2.1×10^{-15}	0.0114	0.0114
ϵ_{12} [−]	-0.0269	-0.0269	-2.1×10^{-15}	-5.2×10^{-16}	0.032	0.032
σ_{11} [MPa]	-25.305	-25.305	24.011	24.011	212.422	212.422
σ_{22} [MPa]	-53.720	-53.720	7.065	7.065	87.757	87.757
σ_{12} [MPa]	-107.557	-107.557	-0.132	-0.132	64.267	64.267

Table 5. Solver comparison (stress and strain) for the imposed stress test

Value	Minimum		Average		Maximum	
	FixedPoint	Polarization	FixedPoint	Polarization	FixedPoint	Polarization
ϵ_{11} [−]	-4.592×10^{-4}	-4.592×10^{-4}	4.556×10^{-5}	4.556×10^{-5}	0.00179	0.00179
ϵ_{22} [−]	-6.954×10^{-4}	-6.954×10^{-4}	-1.331×10^{-5}	-1.331×10^{-5}	3.555×10^{-4}	3.555×10^{-4}
ϵ_{12} [−]	-0.00115	-0.00115	5.898×10^{-7}	5.898×10^{-7}	0.00146	0.00146
σ_{11} [MPa]	-0.886	-0.886	1	1	9.507	9.507
σ_{22} [MPa]	-2.682	-2.682	$3.0.38 \times 10^{-13}$	-7.092×10^{-13}	3.774	3.774
σ_{12} [MPa]	-4.062	-4.062	-2.926×10^{-12}	-3.075×10^{-12}	2.740	2.740

Table 6. Solver comparison (error) for the axial tension tests

Test	Solver	Iterations [-]	Time to solve [s]	Time / iteration [s]
Imposed strain	FFTFixedPoint	5711	755.25	0.1322
	FFTPolarization	201	53.04	0.2639
Imposed stress	FFTFixedPoint	5971	794.36	0.1330
	FFTPolarization	248	63.06	0.2542

SCALABILITY

The nature of the FFT algorithms makes them directly parallelizable. Indeed, all matrix-vector operations only need to be applied at each pixel individually, and the FFTW library used for the FFT operations themselves can be run in parallel as well. In MOSAIC, parallelism is achieved with the OpenMP library [Dagum and Menon, 1998].

Computational times for the imposed strain test and the FFTPolarization solver are reported as a function of the number of threads on Figure 6. These computations were performed on a Linux workstation with 12 individual cores. The speed-up reaches a plateau around half the number of cores of the workstation, which is the expected behavior for this type of analysis.
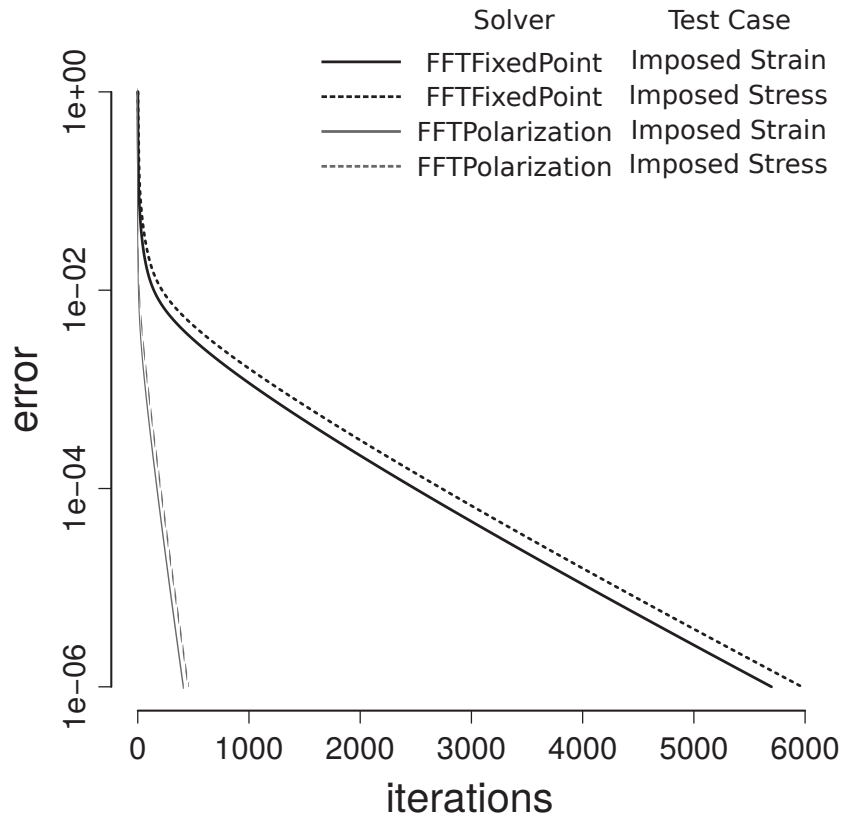
Figure 5. Error of the FFT solvers for the axial tension tests.

PHASE CONTRAST

The convergence properties of FFT schemes depend on the contrast in mechanical properties between the different phases. To test the robustness of these schemes, the imposed strain calculation with the `FFTPolarization` solver are repeated with different values of the mechanical properties for the porosity. The Young's modulus attributed to pixels in the porosity is varied from 1 GPa to 1 MPa.

The number of iterations at convergence and the average axial stress σ_{11} are measured and reported in Figure 7. A value of 0.1 GPa (corresponding to the properties reported in Table 3) provides a good balance between number of iterations and accuracy.
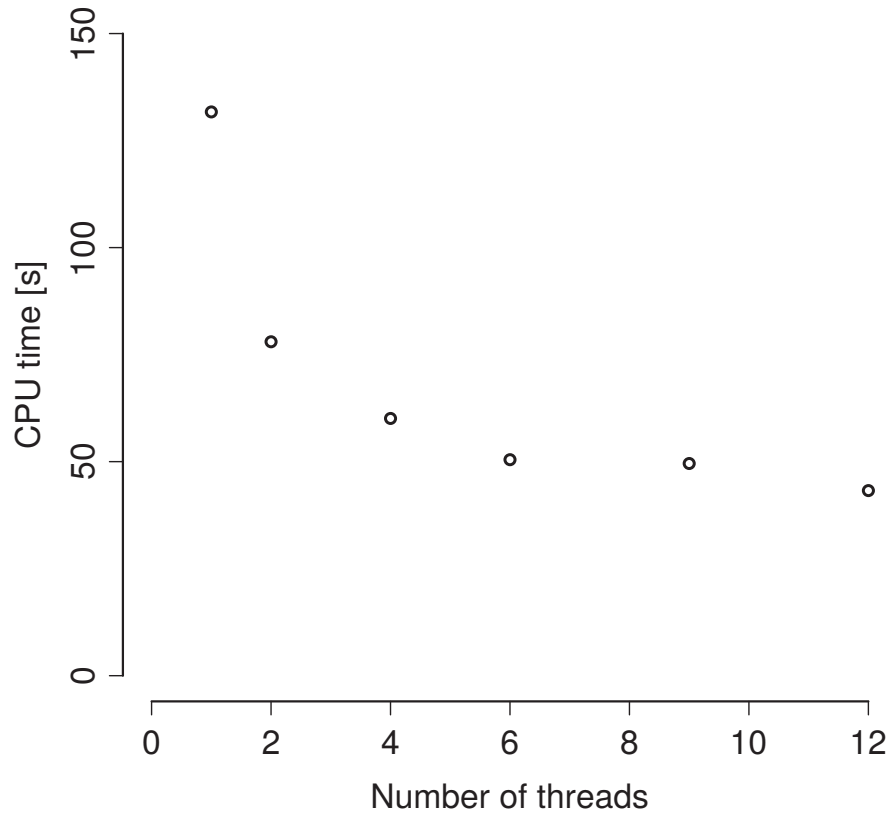
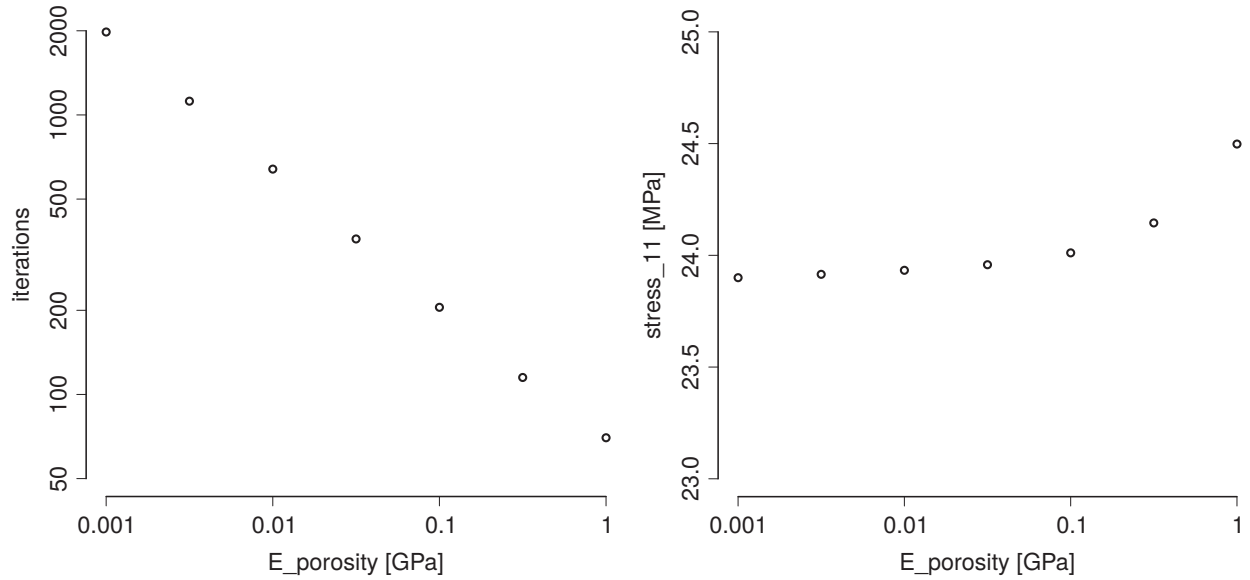**Figure 6. Computational time of the FFT solvers as a function of the number of processors.**

Figure 7. Number of iterations at convergence (left) and average macroscopic stress σ_{11} (right) as a function of the Young's modulus of the porosity.

COMPARISON WITH HOMOGENIZATION SCHEMES

The FFT solvers allow for a full characterization of the homogenized stiffness tensor of the concrete material (for example, by making a strain tension test in each direction). In this specific test, the homogenized stiffness tensor calculated by FFT is found to be (in GPa):

$$\mathbb{C}^{FFT} = \begin{pmatrix} 24.0111 & 7.0656 & -0.1329 \\ 7.0656 & 24.1742 & -0.0859 \\ -0.1329 & -0.0859 & 8.3328 \end{pmatrix} \tag{22}$$

The homogenized tensor is symmetric and almost isotropic. The corresponding mechanical properties are:

$$\mathrm{E}^{FFT} = 21.931 \, [\mathrm{GPa}] \quad , \quad \nu^{FFT} = 0.294 \, [-] \tag{23}$$

For reference, the Voigt-Reuss bounds for the material can be calculated as (see for example [Le Pape et al., 2015] for a refresher on analytical homogenization):

$$\mathrm{E}^{voigt} = 68.132 \, [\mathrm{GPa}] \quad , \quad \nu^{voigt} = 0.4164 \, [-] \tag{24}$$
$$\mathrm{E}^{reuss} = 2.669 \, [\mathrm{GPa}] \quad , \quad \nu^{reuss} = 0.2528 \, [-] \tag{25}$$

The FFT calculations are well within those bounds, which further validates this numerical scheme.

PRELIMINARY ESTIMATION OF CONCRETE RIVE

The `FFTPolarization` solver is used to characterize the apparent RIVE of that concrete, assuming all phases are purely elastic. This is a preliminary simulation to show the capability of the method, and not an accurate prediction of that material sensitivity to RIVE. To do so, one would need a visco-elastic model for the cement paste, and a damage model for both the paste and the minerals.

The expansion of the ankerite and calcite are taken as the maximum values in the IMAC database. These specific data points were collected by [Denisov et al., 2012].

$$\epsilon_{imp}^{ankerite} \quad = \quad \{0.011, \, 0.011, \, 0\} \tag{26}$$
$$\epsilon_{imp}^{calcite} \quad = \quad \{0.001666, \, 0.001666, \, 0\} \tag{27}$$

In order to calculate the average RIVE of that specific concrete, a null macrostress $\Sigma = 0$ is imposed. The solver converged after 300 iterations in 54.44 seconds, which is similar to the previous tests. The average expansion calculated by FFT is measured as:

$$\epsilon_{imp}^{FFT} = \{0.001068, \, 0.001050, \, -0.000023\} \tag{28}$$

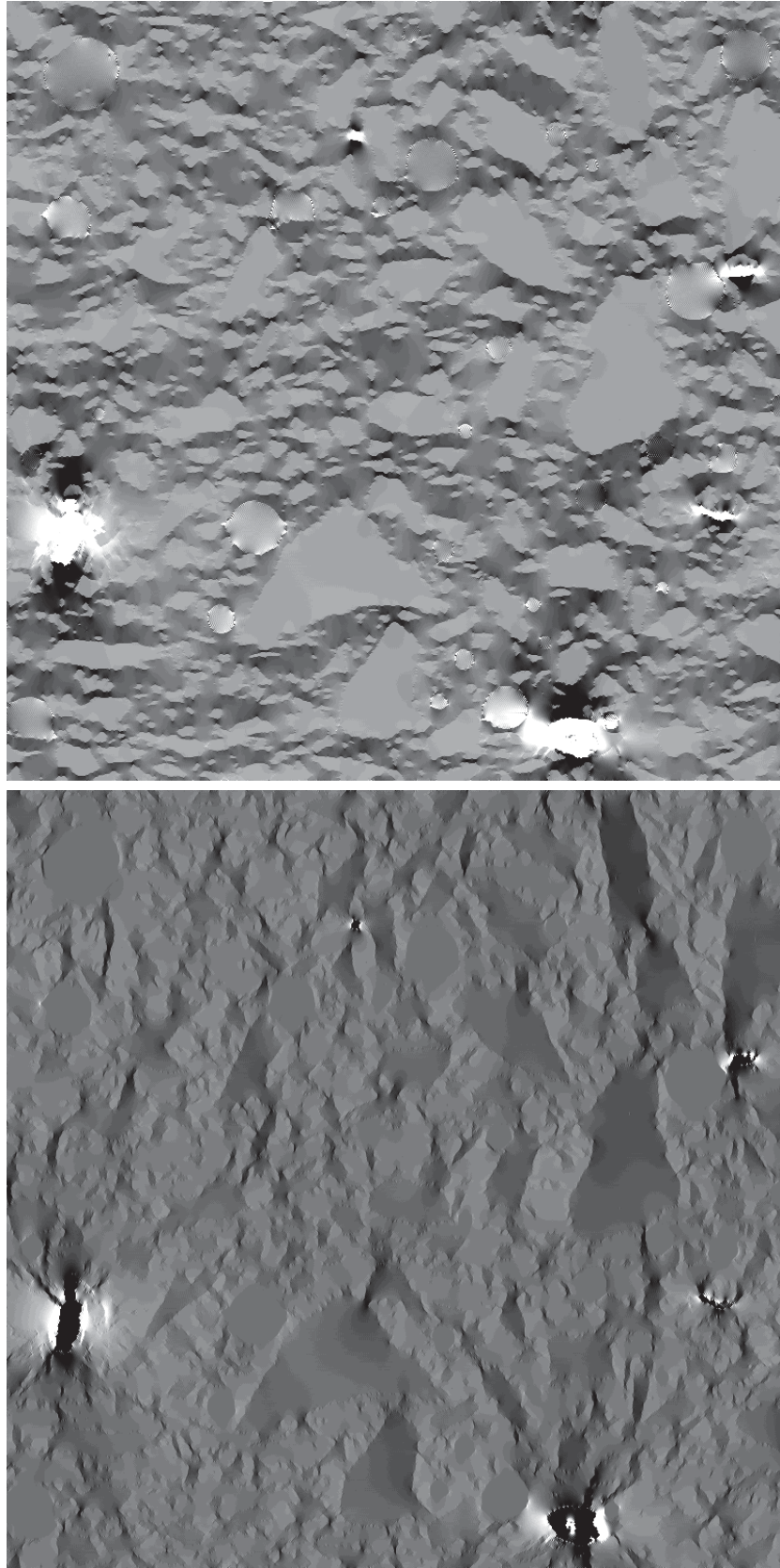Again one can observe that the expansion is almost isotropic.

Figure 8. ϵ_{11} (top) and σ_{11} (bottom) components of the strain and stress fields for the concrete sample subject to RIVE. High values are in white, low values in black.

In these conditions, the minimum and maximum stresses in the material reach particularly high values (up to 800 MPa).

The map of strains and stresses are reported in Figure 8. The highest strains are measured either in the ankerite grains (which has the highest RIVE), or around the edges of the porosity (similar to what was found in the axial tests). The highest tensile stresses are measured around the ankerite grains, themselves subject to very high compressive stresses.

ANISOTROPIC SIMULATION

Calcite and ankerite are both anisotropic materials. As FFT solvers implemented are able to account for anisotropic mechanical properties, as long as the reference medium itself is isotropic.

The simulations above are repeated with anisotropic properties for both the calcite and the ankerite. Due to lack of data, each particle in the phase map (Figure 3) is first randomly oriented in the three-dimensional space. The three-dimensional stiffness tensor is then projected on the two dimensional plane of the simulation. The resulting material properties are shown in Figure 9

The homogenized mechanical properties of that material are calculated with the `FFTPolarization` solver. Number of iterations and computational time are similar (slightly higher) than for the isotropic material.

$$\mathbb{C}^{FFT} = \begin{pmatrix} 24.1740 & 7.0337 & -0.1403 \\ 7.0337 & 24.3974 & -0.0819 \\ -0.1403 & -0.0819 & 8.4435 \end{pmatrix} \tag{29}$$

$$\epsilon_{imp}^{FFT} = \{0.001070, 0.001052, -0.000019\} \tag{30}$$

The results are also very close to the isotropic simulations, and the strain and stress maps are similar to those found in the isotropic case. Notably, there is no differential stress within aggregates of the same mineralogy (pure calcite, or pure ankerite). This is likely due to the fact that the expansion for each mineral ϵ_{imp} remains isotropic in this simulation.

This simulation is a proof of concept that validates the use of FFT solvers for the analysis of RIVE in concrete, notably its ability to account for imposed strains such as RIVE or thermal expansion, or anisotropy of the different mineral phases.
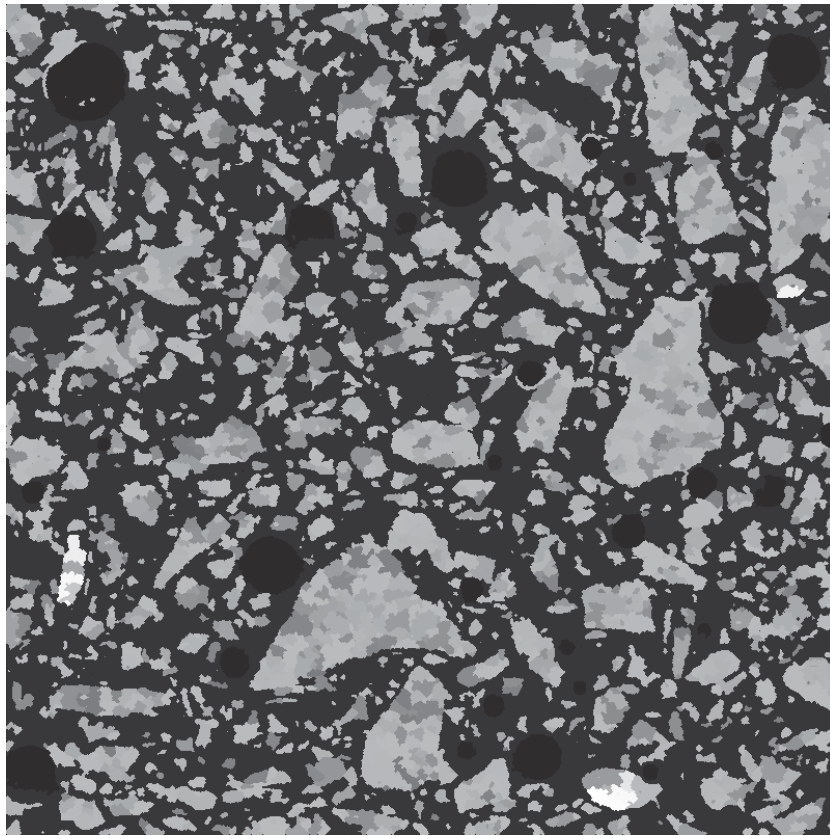
Figure 9. $\mathbb{C}_{1111}$ **component of the stiffness tensor for the anisotropic simulation.**

CONCLUSION

The present report shows two FFT algorithms applicable for the simulation of RIVE in concrete from microstructural characterization techniques such as μ-XRF. These algorithms were validated on analytical examples from the literature, and then applied to concrete microstructures as preliminary simulations. The method can account for imposed eigenstrain (including thermal expansion, RIVE, drying shrinkage, etc) and anisotropic mechanical properties (to simulate crystal grain orientation).

The simulations presented in this report are preliminary studies to showcase the capabilities of the method. For a more realistic depiction of RIVE in concrete, the following developments are required.

- The FFT solvers need to be coupled with a non-linear solver in order to simulate damage in the material. This is required to provide understanding of the material degradation as a function of the irradiation. This can be achieved using the sequential approach developed for irradiated concrete in [Giorla et al., 2017]. A similar approach (coupling of FFT with a non-linear Newton-Raphson solver) was also presented in [Zeman et al., 2017].

- The failure properties of the mineral themselves need to be investigated. At the mineral level, two failure modes must be considered: intragranular cracking (propagation of micro-cracks within each grain) and intergranular cracking (similar debonding between the grains). These two failure modes are observed in thermal damage of rocks (see for example [Wang et al., 1989]). A literature review is required to complement the IMAC database with appropriate experimental data, and additional experiments may be required. Furthermore, the question of the modelling of debonding with FFT requires additional effort (see for example [Li et al., 2012]).

- The crystal orientation of the minerals in concrete need to be characterized. This can be achieved using optical microscopy techniques such as ellipsometry. Knowing the crystal orientation and the amorphization degree of grains in concrete would also help distinguish minerals of the same chemical composition, but different crystal structures (such as quartz and amorphous silica).

- Finally, the question of the anisotropy of RIVE itself needs to be addressed. In most cases, the expansion measured in the literature is the volumetric expansion. Some authors (see for example [Seeberger and Hilsdorf, 1982, Denisov et al., 2012]) also measured changes in lattice parameters as a function of irradiation. Such information, combined with data already contained in the IMAC database, could provide insight on the anisotropy of the expansion itself.

REFERENCES

S. Brisard and L. Dormieux. Fft-based methods for the mechanics of composites: A general variational framework. *Computational Materials Science*, 49(3):663–671, 2010.

L. Dagum and R. Menon. Openmp: an industry standard api for shared-memory programming. *IEEE computational science and engineering*, 5(1):46–55, 1998.

A. Denisov, V. Dubrovskii, and V. Solovyov. *Radiation Resistance of Mineral and Polymer Construction Materials*. ZAO MEI Publishing House, 2012. in Russian.

T. Esselman and P. Bruck. Expected condition of concrete at age 80 of reactor operation. Technical Report A13276-R-001, Lucius Pitkins, Inc., 36 Main Street, Amesbury, MA 01913, September 2013.

D. Eyre and G. Milton. A fast numerical scheme for computing the response of composites using grid refinement. *The European Physical Journal-Applied Physics*, 6(1):41–47, 1999.

K. Field, I. Remec, and Y. Le Pape. Radiation Effects on Concrete for Nuclear Power Plants, Part I: Quantification of Radiation Exposure and Radiation Effects. *Nuclear Engineering and Design*, 282: 126–143, 2015.

M. Frigo and S. Johnson. The design and implementation of FFTW3. *Proceedings of the IEEE*, 93(2): 216–231, 2005. Special issue on "Program Generation, Optimization, and Platform Adaptation".

A. Giorla. Advanced numerical model for irradiated concrete. Technical report, LWRS/M3LW-15OR0403044, ORNL/TM-2015/97. Oak Ridge National Laboratory, 2015.

A. Giorla. Characterization of phases in concrete using micro x-ray fluorescence. Technical report, LWRS/M2LW-17OR0403014, ORNL/TM-2017/237. Oak Ridge National Laboratory, 2017.

A. Giorla, M. Vaitová, Y. Le Pape, and P. Štemberk. Meso-scale modeling of irradiated concrete in test reactor. *Nuclear Engineering and Design*, 295:59–73, 2015.

A. Giorla, Y. Le Pape, and C. Dunant. Computing creep-damage interactions in irradiated concrete. *Journal of Nanomechanics and Micromechanics*, 7(2):04017001, 2017.

H. Graves, Y. Le Pape, D. Naus, J. Rashid, V. Saouma, A. Sheikh, and J. Wall. Expanded material degradation assessment (emda), volume 4: Aging of concrete. Technical report, NUREG/CR-7153, ORNL/TM-2011/545. US Nuclear Regulatory Commission, 2014.

H. Hilsdorf, J. Kropp, and H. Koch. The effects of nuclear radiation on the mechanical properties of concrete. *Special Publication of The American Concrete Institute*, 55:223–254, 1978.

M. Kabel, T. Böhlke, and M. Schneider. Efficient fixed point and newton–krylov solvers for fft-based homogenization of elasticity at large deformations. *Computational Mechanics*, 54(6):1497–1514, 2014.

E. Kröner. Bounds for effective elastic moduli of disordered materials. *Journal of the Mechanics and Physics of Solids*, 25(2):137–155, 1977.

F. Lavergne, K. Sab, J. Sanahuja, M. Bornert, and C. Toulemonde. Investigation of the effect of aggregates' morphology on concrete creep properties by numerical simulations. *Cement and Concrete Research*, 71: 14–28, 2015.

Y. Le Pape. Imac database v. 0.1. – minerals. Technical report, LWRS/M2LW-17OR0403044, ORNL/TM-2016/753. Oak Ridge National Laboratory, 2016.

Y. Le Pape. Imac database v. 0.2. – aggregates. Technical report, LWRS/M3LW-17OR0403045, ORNL/TM-2017/240. Oak Ridge National Laboratory, 2017.

Y. Le Pape, K. Field, and I. Remec. Radiation Effects in Concrete for Nuclear Power Plants - Part II: Perspective from Micromechanical Modeling. *Nuclear Engineering and Design*, 282:144–157, 2015.

Y. Le Pape, A. Giorla, and J. Sanahuja. Combined effects of temperature and irradiation on concrete damage. *Journal of Advanced Concrete Technology*, 14(3):70–86, 2016.

J. Li, S. Meng, X. Tian, F. Song, and C. Jiang. A non-local fracture model for composite laminates and numerical simulations by using the fft method. *Composites Part B: Engineering*, 43(3):961–971, 2012.

B. Liu, D. Raabe, F. Roters, P. Eisenlohr, and R. Lebensohn. Comparison of finite element and fast fourier transform crystal plasticity solvers for texture prediction. *Modelling and Simulation in Materials Science and Engineering*, 18(8):085005, 2010.

J. Michel, H. Moulinec, and P. Suquet. A computational method based on augmented lagrangians and fast fourier transforms for composites with high contrast. *CMES(Computer Modelling in Engineering & Sciences)*, 1(2):79–88, 2000.

J. Michel, H. Moulinec, and P. Suquet. A computational scheme for linear and non-linear composites with arbitrary phase contrast. *International Journal for Numerical Methods in Engineering*, 52(1-2):139–160, 2001.

V. Monchiet and G. Bonnet. A polarization-based fft iterative scheme for computing the effective properties of elastic composites with arbitrary contrast. *International Journal for Numerical Methods in Engineering*, 89(11):1419–1436, 2012.

H. Moulinec and F. Silva. Comparison of three accelerated fft-based schemes for computing the mechanical response of composite materials. *International Journal for Numerical Methods in Engineering*, 97(13): 960–985, 2014.

H. Moulinec and P. Suquet. A fast numerical method for computing the linear and nonlinear mechanical properties of composites. *Comptes rendus de l'Académie des sciences. Série II, Mécanique, physique, chimie, astronomie*, 318(11):1417–1423, 1994.

H. Moulinec and P. Suquet. A numerical method for computing the overall response of nonlinear composites with complex microstructure. *Computer methods in applied mechanics and engineering*, 157(1-2):69–94, 1998.

T. Rosseel, I. Maruyama, Y. Le Pape, O. Kontani, A. Giorla, I. Remec, J. Wall, M. Sircar, C. Andrade, and M. Ordonez. Review of the current state of knowledge on the effects of radiation on concrete. *Journal of Advanced Concrete Technology*, 14(7):368–383, 2016.

J. Seeberger and H. Hilsdorf. Einfluss von radioaktiver strahlung auf die festigkeit und struktur von beton. Technical Report NR2505, Institüt fur Massiubau und Baustofftechnologie, Arbeitlung Boustofftechnologie, Universität Karlsruhe, Germany, 1982.

E. Tajuelo Rodriguez. Documenting and imaging multiple samples and testing the performance of the micro-xray fluorescence instrument: Status report. Technical report, LWRS/M3LW-17OR0403013, ORNL/TM-2017/104. Oak Ridge National Laboratory, 2017.

H. Wang, B. Bonner, S. Carlson, B. Kowallis, and H. Heard. Thermal stress cracking in granite. *Journal of Geophysical Research: Solid Earth*, 94(B2):1745–1758, 1989.

J. Zeman, J. Vondřejc, J. Novák, and I. Marek. Accelerating a fft-based solver for numerical homogenization of periodic media by conjugate gradients. *Journal of Computational Physics*, 229(21):8065–8071, 2010.

J. Zeman, T. Geus, J. Vondřejc, R. Peerlings, and M. Geers. A finite element perspective on nonlinear fft-based micromechanical simulations. *International Journal for Numerical Methods in Engineering*, 2017.